Mechanism and Kinetics of Aztreonam Hydrolysis Catalyzed by Class–C β–Lactamase: A Temperature Accelerated Sliced Sampling Study

Shalini Awasthi,[†] Shalini Gupta,[†,‡] Ravi Tripathi,[†,¶] and Nisanth N.Nair[*,†]

†*Department of Chemistry, Indian Institute of Technology, Kanpur, India*

‡*Current address: Department of Biology, Massachusetts Institute of Technology, Cambridge, Massachusetts, USA*

¶*Current Address: Lehrstuhl für Theoretische Chemie, Ruhr Universität, Bochum, Germany*

E-mail: nnair@iitk.ac.in

Abstract

Enhanced sampling of large number of collective variables (CVs) is inevitable in molecular dynamics (MD) simulations of complex chemical processes such as enzymatic reactions. Due to the computational overhead of hybrid quantum mechanical/molecular mechanical (QM/MM) based (MD) simulations, especially together with density functional theory (DFT), predictions of reaction mechanism and estimation of free energy barriers have to be carried out within few tens of picoseconds. We show here that the recently developed Temperature Accelerated Sliced Sampling (TASS) method allows one to sample large number of CVs, thereby enabling us to obtain rapid convergence in free energy estimates in QM/MM MD simulation of enzymatic reactions. Moreover, the method is shown to be efficient in exploring flat and broad free energy basins that commonly occur in enzymatic reactions. We demonstrate this by studying deacylation and reverse acylation reactions of aztreonam drug catalyzed by a class-C β lactamase (CBL) bacterial enzyme. Mechanistic details and nature of kinetics of aztreonam hydrolysis by CBL are elaborated here. The results of this study point to characteristics of the aztreonam drug that are responsible for its slow hydrolysis.

Introduction

Enhanced sampling molecular dynamics (MD) techniques are widely used to model long time scale chemical transformations occurring in molecular systems.[1–3] In most of these techniques, barrier crossing processes are accelerated by applying bias potentials along certain *a priori* chosen coordinates (which are called collective variables or CVs in abbreviation hereafter).[4–16] However, the efficiency of sampling is limited by the number of chosen CVs.[17–19] In practical applications of popular enhanced sampling techniques such as metadynamics[4] and umbrella sampling,[20] the number of CVs is often restricted to two and seldom three and above; see also Refs.[21–24] and references therein. While modeling complex chemical problems, such the enzymatic reactions considered in this work, one requires more than

two CVs to be sampled. In enzymatic reactions, other than the main bond breaking and bond formation conformational changes occurring at the active site, the changes in the side chain conformations within the reaction timescale, structural changes of water molecules in the active site, hydrogen bond breaking/formation events taking place in the reactive center etc. contribute to the free energy estimates and to the mechanism of the reaction. This necessitates sampling of more CVs to accelerate such conformational changes within the simulation time. Several attempts have been made in the literature to overcome the limitation of number of CVs in sampling. Such methods employ strategies such as replica exchange based tempering,[25,26] temperature acceleration of CVs,[10,27] independent or differential sampling of low–dimensional CV space[28–30] to construct high-dimensional free energy surface and variational sampling.[31,32]

Here we focus on the approach we introduced recently called Temperature Accelerated Sliced Sampling (TASS).[30] The main aim here is to apply the TASS approach for sampling large number of CVs for a realistic problem and to present its efficiency in using with *ab initio* based MD simulations. In particular, here we report an extensive application of the TASS approach in studying complex enzymatic reactions using computationally intensive density functional theory (DFT) based hybrid quantum-mechanical/molecular mechanical (QM/MM) MD simulations. One of the important features of the TASS method is that it can explore broad and unbound free energy basins, which is frequently encountered in A+B type of reactions (such as hydrolysis reaction) or reactions in weakly bound complexes (as in a Michaelis complex).[30,33]

These features of the TASS method are as a result of combining high temperature sampling and biased sampling in a special way. The bias potential in TASS composes of one–dimensional umbrella sampling and one–dimensional metadynamics biases applied on different CVs; see Fig. 1 for a schematic description of the TASS approach. The Lagrangian used

in TASS is of the form

$$\begin{aligned}\mathcal{L}_h\left(\mathbf{R},\dot{\mathbf{R}},\mathbf{s},\dot{\mathbf{s}}\right) &= \mathcal{L}_0\left(\mathbf{R},\dot{\mathbf{R}}\right) \\ &- \sum_{\alpha=1}^{n}\left[\frac{1}{2}\mu_\alpha\dot{s}_\alpha^2+\frac{k_\alpha}{2}\left(S_\alpha(\mathbf{R})-s_\alpha\right)^2\right] \\ &- W_h^{\mathrm{b}}(s_1)-V_h^{\mathrm{b}}(s_2,t) \\ &+ \mathrm{bath}(\dot{\mathbf{R}};T)+\mathrm{bath}(\dot{\mathbf{s}};\tilde{T})\end{aligned} \tag{1}$$

where $\mathcal{L}_0$ is the Lagrangian of the physical system. Here $h = 1, \cdots, M$ is the index for different copies of the system, differing in the umbrella bias potential

$$W_h^{\mathrm{b}}(s_1) = \frac{\kappa_h}{2}\left(s_1 - s_1^{0,h}\right)^2$$

along the coordinate s_1. Here the bias potential of an umbrella window h is centered at a suitably chosen value $s_1^{0,h}$. The collective variables $\{S_\alpha\}$ is the set of CVs which are functions of nuclear coordinates $\mathbf{R}$, and $\alpha = 1, \cdots, n$, with $n \geq 2$. We define n auxiliary variables $\{s_\alpha\}$ which are coupled to $\{S_\alpha\}$ by harmonic potentials as shown in (1). A well-tempered form of the bias potential $V_h^{\mathrm{b}}(s_2,t)$ is added[15] where the bias potential is constructed as a function of time by summing the Gaussian repulsive potentials of varying heights deposited in discrete time intervals along $s_2(t)$:

$$V^{\mathrm{b}}(s_2,t) = \sum_{\tau<t} w_\tau \exp\left[-\frac{\left\{s_2 - s_2(\tau)\right\}^2}{2(\delta s)^2}\right]. \tag{2}$$

The parameters w_τ and δs control the height and the width of the individual Gaussian functions deposited at time τ, and[15]

$$w_\tau = w_0 \exp\left[-\frac{V^{\mathrm{b}}(s_2,t)}{k_{\mathrm{B}}\,\Delta T}\right] \tag{3}$$

where w_0 is the initial Gaussian height parameter, ΔT is the tempering parameter in the

units of Kelvin, and k_{B} is the Boltzmann constant. Two temperature baths are introduced, where the system variables are kept at a physically relevant temperature T, while the auxiliary degrees of freedom $\{s_1, s_2, \cdots, s_n\}$ are maintained at a higher temperature $\tilde{T}$. The parameters $\{\mu_\alpha\}$ and $\{k_\alpha\}$ are selected in such a manner that adiabatic septation between between the auxiliary and the physical subsystems is maintained and $\{S_\alpha\}$ and $\{s_\alpha\}$ variables follow each other.

In this way, the TASS approach accelerates the CVs by a combination of umbrella sampling bias, metadynamics bias, and temperature. This approach is thus helpful to explore high dimensional free energy landscapes by the virtue of temperature acceleration, and this method becomes advantageous when the free energy basins are broad or unbound by the virtue of umbrella restraints $W_h^{\mathrm{b}}(s_1)$. In TASS, the free energy surface is computed as,

$$F(\mathbf{s}) = -\frac{1}{\tilde{\beta}} \ln \tilde{P}(\mathbf{s}) \ , \tag{4}$$

akin to the temperature accelerated or driven-adiabatic free energy dynamics,[2,10,27] where $\tilde{\beta} = 1/(k_{\mathrm{B}}\tilde{T})$ and k_{B} is the Boltzmann constant. Here the probability $\tilde{P}(\mathbf{s})$ is computed in a self consistent manner using the weighted histogram analysis method (WHAM)[34,35] as

$$\tilde{P}(\mathbf{s}) = \frac{\sum_{h=1}^{M} n_h \tilde{P}_h(\mathbf{s})}{\sum_{h=1}^{M} n_h \exp[\tilde{\beta} f_h] \exp[-\tilde{\beta} W_h^{\mathrm{b}}(s_1)]} \ , \tag{5}$$

with

$$\exp[-\tilde{\beta} f_h] = \int ds_1 \exp[-\tilde{\beta} W_h^{\mathrm{b}}(s_1)] \tilde{P}(\mathbf{s}) \ , \tag{6}$$

and

$$\tilde{P}_h(\mathbf{s}') = \frac{\int d\tau \, A_h(\tau) \prod_\alpha^n \ \delta(s_\alpha(\tau) - s'_\alpha)}{\int d\tau \, A_h(\tau)} \ , \tag{7}$$

having the reweighting factor[12,36,37]

$$A_h(\tau) = \exp\left[\tilde{\beta}\left\{V_h^{\rm b}(s_2(\tau),\tau) - c_h(\tau)\right\}\right]$$

with

$$c(t) = \frac{1}{\tilde{\beta}} \ln\left[\frac{\int ds_2 \exp[\tilde{\beta}\gamma V^{\rm b}(s_2,t)]}{\int ds_2 \exp[\tilde{\beta}\,(\gamma-1)\,V^{\rm b}(s_2,t)]}\right] \ ,$$

and

$$\gamma = (\tilde{T} + \Delta T)/\Delta T \ ,$$

where ΔT is the tempering parameter in well-tempered metadynamics, as discussed before.

Using TASS QM/MM MD simulations, here we study the hydrolysis of aztreonam drug molecule within the active site of a Class-C β-lactamase (CBL) bacterial enzyme, with the aim to understand the molecular mechanism of such enzymatic reactions that result in antibiotic resistance in bacteria. Antibiotic resistance has become a major concern in the treatment of infectious diseases.[38–43] Most of the antibacterial drugs are inhibitors of penicillin binding proteins (PBPs) that are crucial for the biosynthesis of the bacterial cell wall. Antibiotic resistance originates when bacteria acquire resistance against β–lactam antibiotics by expressing β–lactamase enzymes that could catalyze the hydrolysis of β–lactam antibiotics, thereby making the drugs ineffective.[44,45]

CBL enzymes are among the four classes (A,B,C,D) of β–lactamases classified based on sequence similarity.[46] CBLs are commonly found in Gram negative bacteria and they use a serine residue present in their active site for catalyzing the hydrolysis of β–lactam antibiotics. There are two main reaction steps in the hydrolysis of a drug molecule by CBL;[47–49] see Fig. 2. (1) Acylation reaction: Michaelis complex (**ES**) undergoes acylation, wherein the active site serine forms a covalent bond with a ring carbon to allow for opening of the β–lactam ring by C-N bond breakage, forming **EI**. (2) Deacylation reaction: Covalent bond between

the ring–opened drug and the serine in **EI** is cleaved by water mediated hydrolysis to form **EP**.

Stability of the reaction intermediates and the free energy barriers for the elementary steps influence the overall turnover of the drug hydrolysis reaction. If the deacylation step is slow, especially in comparison to acylation and reverse acylation reactions, then the catalytic serine remains covalently bound to the drug molecule for a long time. In such cases, the drug substrate acts as an inhibitor for CBL, thus increasing the effectiveness of the drug. On the other hand, if deacylation reaction proceeds quickly, the catalytic serine is unmasked rapidly, thereby increasing the turnover of drug hydrolysis. For simplicity, the overall hydrolysis reaction can be casted by the kinetic model,

$$\mathbf{E} + \mathbf{S} \underset{k_{-1}}{\overset{k_1}{\rightleftharpoons}} \mathbf{ES} \underset{k_{-2}}{\overset{k_2}{\rightleftharpoons}} \mathbf{EI} \xrightarrow{k_3} \mathbf{E} + \mathbf{P}$$

where **E**, **S**, and **P** are enzyme, substrate, and product, and **ES** and **EI** are enzyme-substrate non-covalent and covalent complexes, respectively. For a substrate that is an inhibitor, deacylation is slow and $k_3 < k_2$. Further, when $k_3 < k_{-2}$, then reverse acylation reaction takes place as well and can influence the equilibrium concentrations of free substrate and enzyme in solution.[50]

An understanding of the mechanism of the acylation and deacylation reactions and their kinetics, can provide valuable inputs for the design of novel inhibitors for CBL.[51,52] Several experimental and theoretical studies, have contributed to the understanding that active site residues such as Lys_{67}, Tyr_{150}, Asn_{152}, Ala_{220}, and Lys_{315} that are structurally adjacent to the catalytic Ser_{64} play crucial roles in the catalytic process.[53–57] Based on these studies, numerous hypothesis have been put forth with regard to mechanism of hydrolysis. The major challenge to understanding catalytic mechanism has been the identification of active site CBL residues that act as the general base and as the proton donor during the acylation and the deacylation steps.

Cephalothin is a fast hydrolyzing drug when catalyzed by CBL,[58] and thus $k_{\mathrm{cat}} \approx k_2$ is expected.[59] To the contrary, aztreonam (Fig. 2b) is slowly hydrolyzed and deacylation is

expected to be the rate determining step in its hydrolysis. Kinetic studies by Galleni et al.[58] have shown that aztreonam behaves as a transient inhibitor of CBL. The slow hydrolysis of aztreonam has been attributed to the acyl-enzyme **EI** complex blocking the entry of catalytic water molecules.[60] The role of SO_3^{2-} in slowing down the water entry to the active site is also proposed.[61] However, these proposals are in contradiction to the QM/MM MD simulation data of CBL–aztreonam acyl–enzyme complex,[62] where catalytic water was found within the active site.[62] Detailed mechanistic study of aztreonam deacylation and reverse acylation, and computation of free energy barriers for these reactions are therefore important to scrutinize the origins of the slow hydrolysis of aztreonam. This in turn could pave way in the design of new inhibitors. In this respect, we investigate here the hydrolysis of aztreonam catalyzed by CBL in great detail.

Mechanism and the free energy barriers for the acylation reaction **ES**→**EI** were reported in our earlier study,[62] and thus investigation of this step is not repeated here. In this work, we simulate (a) **EI**→**ES** (reverse acylation) (b) **EI** →**EP** (deacylation), where **EP** is the enzyme-product non-covalent complex. The latter reaction is performed in three steps: (b.1) **EI**→**EIb**; (b.2) **EIb**→**EI**; (b.3) **EIb**→**EP**; see Fig. 3. The results of this study, in combination with the knowledge of the mechanism and free energy barriers for acylation reaction step from Ref.,[62] we present the complete mechanism and kinetics of aztreonam hydrolysis by CBL.

Methods and Models

Initial structure of the acyl-enzyme complex **EI** formed by aztreonam and CBL was taken from our previous work,[62] wherein the structure was formed after the metadynamics simulation of **ES**→**EI** and the **ES** structure was constructed based on the PDB ID 1FR6.[63] The whole system was composed of the protein-drug complex solvated with 15041 TIP3P water molecules, five Na^+ and six Cl^- ions, contained in a periodic simulation box of size

87×82×70 Å^3. Hybrid QM/MM canonical ensemble MD simulations were performed using the CPMD/GROMOS interface program.[64] Here, the side chains of Ser_{64}, Lys_{67}, Tyr_{150}, Lys_{315}, aztreonam molecule, and four water molecules within the active site region were treated using density functional theory (DFT). The rest of the protein was treated using the param99 AMBER force-field[65] and for the solvent molecules TIP3P water model was employed. Bonds between QM and MM atoms at the boundaries are capped by H atoms. The QM/MM boundaries were introduced between C_δ and C_ϵ for Lys_{315} and Lys_{67}, while they were between C_α and C_β for Ser_{64} and Tyr_{150}. The capping H atoms were constrained to stay along the QM–MM bond throughout the dynamics. The size of the QM supercell was 27×21×21 Å^3. The DFT computations were carried out using plane-wave basis set with a plane-wave cutoff of 25 Ry for the wave function expansion. We chose the PBE[66] density functionals as in our previous work.[62] Ultrasoft pseudopotentials[67] were used to treat the core electrons of all the QM atoms. We used the QM/MM electronic coupling scheme developed by Laio et al.,[68] where the point charges of all the MM atoms within 15 Å of a QM charge density was included to explicitly interact with the QM charge density. The rest of the point charges of MM atoms were allowed to interact with the multipole expansion of charge density up to the quadrapole. During MD simulations, all atoms, including those of solvent, were allowed to move. However, while simulating the reverse acylation reaction, we have applied restraints on the boundary QM water molecules such that they cannot exchange with MM water molecules; see SI Section 1 for details. Nosé–Hoover chains thermostat[69] was used to maintain the temperature at 300 K. Car–Parrinello MD was performed for QM atoms.[68,70] Orbital degrees of freedom were given a fictitious mass of 700 a.u. and the time step for integrating the equations of motion was 0.125 fs.

We used the TASS method with the Lagrangian in Eqn.1, as implemented in the CPMD code.[30,64] The temperature of the auxiliary variables ($\tilde{T}$) was set to 1000 K using an over-damped Langevin thermostat with a frictional coefficient of 0.4 fs^{-1}. The parameters μ_α and k_α for all the variables were set to 50 a.m.u. and 1.2 × 10^3 kcal mol^{-1}, respec-

tively. The umbrella restraint potentials for all the umbrella windows were using $\kappa_h = 4.5 \times 10^2$ kcal mol^{-1} Å^{-2}. Also, for every umbrella window, the bias $V^{\mathrm{b}}(s_2, t)$ was updated every 19 fs and the other parameters related to this bias potential were $w_0 = 0.6$ kcal mol^{-1}, $\delta s = 0.05$, and $\Delta T = 2000$ K. In our simulations, we used two types of CVs: distance between two atoms A and B, $d[\mathrm{A} - \mathrm{B}]$ and coordination number between an atom A and a number of other atoms $\mathrm{B}_1, \cdots \mathrm{B}_m$, $C[\mathrm{A} - \{\mathrm{B}_1, \cdots, \mathrm{B}_m\}]$. Description on the definition of the coordination number CVs and the parameters used to define these functions are given in SI Section 2. The other details of the chosen CVs will be discussed in the next section. The free energy surfaces are computed using the Eqns.7 and 4.

Results

Reverse Acylation of the Acyl–Enzyme Complex

In order to understand the kinetics of hydrolysis of aztreonam catalyzed by CBL, it is crucial to compare the free energy barrier of reverse acylation (**EI**→**ES**) with respect to deacylation (**EI**→**EP**), i.e. to juxtapose k_{-2} and k_3. For this we started our QM/MM simulations with the **EI** structure. We realized that to simulate the reverse acylation reaction, eight CVs would be appropriate (see Fig. 2b,c and Fig. 4b for labelling): a) distance between AztN_1 and AztC_2, $d[\mathrm{AztN}_1 - \mathrm{AztC}_2]$; b) coordination number of AztN_1 to its hydrogen and hydrogen of W_1, $C[\mathrm{AztN}_1 - \{\mathrm{AztN}_1\mathrm{H}_1, \mathrm{W}_1\mathrm{H}\}]$, where W_1 is the water molecule that is found close to the drug molecule within the **EI** structure (see also Fig. 4b);[62] c) coordination number of $\mathrm{W}_1\mathrm{O}$ to its hydrogens, $C[\mathrm{W}_1\mathrm{O} - \mathrm{W}_1\mathrm{H}]$; d) coordination number of $\mathrm{W}_1\mathrm{O}$ to hydrogen of AztN_1, $C[\mathrm{W}_1\mathrm{O} - \mathrm{AztN}_1\mathrm{H}_1]$; e) coordination number of $\mathrm{Tyr}_{150}\mathrm{O}_\eta$ to hydrogens of W_1 and hydrogen of AztN_1, $C[\mathrm{Tyr}_{150}\mathrm{O}_\eta - \{\mathrm{AztN}_1\mathrm{H}_1, \mathrm{W}_1\mathrm{H}\}]$; f) distance between $\mathrm{Ser}_{64}\mathrm{O}_\gamma$ to AztC_2, $d[\mathrm{Ser}_{67}\mathrm{O}_\gamma - \mathrm{AztC}_2]$; g) coordination number of $\mathrm{Ser}_{64}\mathrm{O}_\gamma$ to the terminal protons of $\mathrm{Lys}_{67}\mathrm{N}_\zeta$, $C[\mathrm{Ser}_{64}\mathrm{O}_\gamma - \mathrm{Lys}_{67}\mathrm{N}_\zeta\mathrm{H}_\zeta]$; h) coordination number of $\mathrm{Lys}_{67}\mathrm{N}_\zeta$ to its protons, $C[\mathrm{Lys}_{67}\mathrm{N}_\zeta - \mathrm{Lys}_{67}\mathrm{N}_\zeta\mathrm{H}_\zeta]$. These CVs are based on the chemical intuition that the

mechanism of **EI**→**ES** is along the same path (but in the reverse order) for **ES**→**EI**, which was reported by us in our earlier work.[62] All the eight CVs were kept at high temperature ($\tilde{T}$ = 1000 K) to enhance their sampling, as discussed in the previous section. Among the CVs chosen, $d[\mathrm{AztN_1}-\mathrm{AztC_2}]$ coordinate was chosen for applying the umbrella bias potential. Along this coordinate, umbrella windows were placed from 1.3 Å to 2.9 Å at an interval of 0.1 Å. As we foresee broad free energy landscape along this CV in the **EI** basin (due to absence of a bond between $\mathrm{AztN_1}$ and $\mathrm{AztC_2}$), we chose this coordinate in the umbrella sampling. The coordinate, $C[\mathrm{AztN_1} - \{\mathrm{AztN_1H_1}, \mathrm{W_1H}\}]$ was sampled to accelerate the proton transfer between $\mathrm{AztN_1}$ and water. We sampled this CV by applying metadynamics bias potential, since a broad/unbound basin along this CV is not anticipated in the reactant basin, but a substantially high barrier is expected to break the Azt $\mathrm{N_1}$–$\mathrm{H_1}$ bond. The choice of CVs $C[\mathrm{W_1O} - \mathrm{W_1H}]$ and $C[\mathrm{W_1O} - \mathrm{AztN_1H_1}]$ was to enhance the deprotonation and protonation of $\mathrm{W_1}$. The CV, $C[\mathrm{Tyr_{150}O_\eta} - \{\mathrm{AztN_1H_1}, \mathrm{W_1H}\}]$, was selected to sample two possible routes through which $\mathrm{Tyr_{150}}$ can take a proton from either $\mathrm{W_1}$ or $\mathrm{AztN_1}$. As the formation of **ES** from **EI** involves breaking of the covalent bond between $\mathrm{Ser_{67}O_\gamma}$ and $\mathrm{AztC_2}$, we have chosen $d[\mathrm{Ser_{67}O_\gamma} - \mathrm{AztC_2}]$ as another CV. A proton transfer from $\mathrm{Lys_{67}}$ to $\mathrm{Ser_{64}O_\gamma}$ is also expected[62] considering the proximity of $\mathrm{Lys_{67}}$ and $\mathrm{Ser_{64}}$ in the **EI** structure. To facilitate the protonation of $\mathrm{Ser_{64}O_\gamma}$ and deprotonation of $\mathrm{Lys_{67}}$, we have enhanced sampled the coordinates $C[\mathrm{Ser_{64}O_\gamma} - \mathrm{Lys_{67}N_\zeta H_\zeta}]$ and $C[\mathrm{Lys_{67}N_\zeta} - \mathrm{Lys_{67}N_\zeta H_\zeta}]$.

We were successful in simulating the reverse acylation with the above defined CVs using the TASS method. The convergence of free energy barriers as a function of simulation length per umbrella window is given in Table S2. The converged free energy surface projected on the $d[\mathrm{AztN_1} - \mathrm{AztC_2}]$ and $C[\mathrm{AztN_1} - \{\mathrm{AztN_1H_1}, \mathrm{W_1H}\}]$ coordinates is shown in Fig. 4a. The converged free energy barrier for **EI** → **EIa** was found to be 25.6 kcal $\mathrm{mol^{-1}}$. Interestingly, during this reaction, an intermediate **EIa** was observed akin to our previous report on acylation mechanism.[62] In this intermediate, $\mathrm{C_2}$–$\mathrm{SerO_\gamma}$ bond is not completely broken, while the Azt $\mathrm{N_1}$–$\mathrm{C_2}$ bond formation has occurred and deprotonation of Azt $\mathrm{N_1}$ is

complete. We find that the proton transfer to $Tyr_{150}O_{\eta}$ occurs through water molecule W_1; at first Azt N_1H_1 is transferred to W_1 and simultaneously, a proton of W_1 is transferred to $Tyr_{150}O_{\eta}$. Free energy barriers for **EIa** $\rightarrow$ **ES** and **EIa** $\rightarrow$ **EI** were also computed from the same simulation and are 3.5 kcal mol^{-1} and 4.1 kcal mol^{-1}, respectively. These results are consistent with the acylation mechanism and free energy barriers reported previously.[62] Also, from Fig. 4a it is clear that the reactant basin is broad along the $d[AztN_1 - AztC_2]$, as anticipated.

On analyzing the umbrella windows in the **EI** basin, we noted that the distance between $Tyr_{150}O_{\eta}$ and $AztN_1$ is about 6 Å, and W_1 water molecule is trapped between the two residues. Thus, a direct proton transfer from $AztN_1$ to $Tyr_{150}O_{\eta}$ could be ruled out. Although, we have considered the possibility of a direct proton transfer from $AztN_1$ to $Tyr_{150}O_{\eta}$, we could only find W_1 mediated proton transfer mechanism in our simulation.

In accordance with the findings of Refs.,[62,71] we observed frequent proton transfer between $Tyr_{150}O_{\eta}$ and $Lys_{67}N_{\zeta}$ in the **EI** structure. While analyzing the trajectories, we observed that Lys_{67} has higher probability of being protonated. As the reaction proceeds from **EI** to **EIa**, the hydrogen bonding interactions between Lys_{67} and $Tyr_{150}O_{\eta}$ breaks, and the protonated Lys_{67} makes hydrogen bonding interactions with Ser_{64}. During the **EIa**$\rightarrow$**ES**, elongation in $Ser_{64}O_{\gamma}$–Azt C_2 bond was noticed, which was followed by proton transfer from $Lys_{67}N_{\zeta}$ to $Ser_{64}O_{\gamma}$, resulting in **ES**. We also find that in all the umbrella windows going from **EI**$\rightarrow$**ES**, Lys_{315} retains its hydrogen bonding interaction with Tyr_{150}.

Mechanism of Deacylation Reaction

In the next step, we looked at the deacylation reaction, **EI**$\rightarrow$**EP**, to estimate the free energy barrier for the reaction. Deacylation of the **EI** complex is shown to take place in two steps in the previous study.[71] First step involves the formation of the tetrahedral intermediate **EIb**, by the nucleophilic attack of W_1 on Azt C_2 after getting activated by Tyr_{150}. In the subsequent step, **EIb**$\rightarrow$**EP**, a proton transfer to $Ser_{64}O_{\gamma}$ from Lys_{67} leads to the dissociation

of the bond between Azt C_2 and $Ser_{64}O_\gamma$.

Tetrahedral Intermediate EIa Formation

We briefly reported earlier that this reaction step can be modeled efficiently using the TASS method.[30] Here we discuss the results of that simulation in detail.

A number of experimental studies have suggested that deprotonated form of Tyr_{150} acts as the base in activating the hydrolyzing water molecule.[57,63,72–76] On the other hand, the works of Chen et al.[77] and Kato-Toma et al.[78] have favored the neutral form of Tyr_{150} in the **EI** structure. Based on the crystal structure of an **ES** intermediate, Shoichet and coworkers suggested that either anionic Tyr_{150} or the substrate β-lactam N acts as the base.[74] Mobashery and coworkers also supported substrate–assisted hydrolysis mechanism for deacylation, wherein the β–lactam N acts as the base.[79] QM/MM computations by Gherman et al. found a concerted mechanism, where Tyr_{150} activates the catalytic water and the former transfers its proton to Lys_{67}.[80] A computational study by Hata et al.[81] also concluded that Tyr_{150} is the general base while Lys_{67} is involved in proton transfer to Ser_{64}. Our recent work[59] on cephalothin hydrolysis by CBL using QM/MM MD techniques also confirmed the same deacylation mechanism.

To model the **EI**→**EIb** here, we have essentially followed the same mechanism as we found for the deacylation of cephalothin by CBL[71] where Tyr_{150} acts as the base that activates hydrolyzing water molecule W_1. This is based on the stable interaction between Tyr_{150} and W_1 throughout the equilibrium MD simulation of **EI**. We chose four CVs in order to simulate **EI**→**EIb** (see Fig. 2b,c and Fig. 5c for labeling): a) coordination number of $Tyr_{150}O_\eta$ to hydrogens of W_1, $C[Tyr_{150}O_\eta - W_1H]$; b) distance between $AztC_2$ and W_1O, $d[AztC_2 - W_1O]$; c) the distance $Tyr_{150}O_\eta$ to $Lys_{67}N_\zeta$, $d[Tyr_{150}O_\eta - Lys_{67}N_\zeta]$; d) the distance $Tyr_{150}O_\eta$ to $Lys_{315}N_\zeta$, $d[Tyr_{150}O_\eta - Lys_{315}N_\zeta]$. All the four CVs were treated at high temperature (1000 K). We chose the $d[AztC_2 - W_1O]$ CV to enhance the formation of $AztC_2 - W_1O$ bond, i.e. the nucleophilic attack of W_1 on Azt C_2. This CV was selected for applying the

umbrella restraint because in the reactant state, no bond exists between W_1O and Azt C_2, and thus a broad basin is expected. We placed umbrella restraints from 1.3 Å to 5.1 Å at an interval of 0.1 Å. We chose the $C[Tyr_{150}O_\eta - W_1H]$ to accelerate the sampling of W_1H transfer to $Tyr_{150}O_\eta$. This coordinate was enhanced sampled by metadynamics bias because W_1 is always found hydrogen bonded to $Tyr_{150}O_\eta$, and thus we do not expect a broad basin along this coordinate. In the equilibrium MD simulation of **EI**, proton transfer between Lys_{67} and Tyr_{150} was frequently seen. Thus deprotonation of Tyr_{150} has to be sampled in order to simulate the activation of W_1 by Tyr_{150}. In order to do that the CVs $d[Tyr_{150}O_\eta - Lys_{67}N_\zeta]$ and $d[Tyr_{150}O_\eta - Lys_{315}N_\zeta]$ were taken here. These CVs could aid to explore different conformations of Tyr_{150}, Lys_{67}, and Lys_{315} within the active site.

The **EI**→**EIb** reaction was observed successfully using the TASS method. The convergence of the free energy barrier for this process was monitored by increasing the simulation time of every umbrella window, and in 8 ps per umbrella window a satisfactory convergence was achieved; see SI Table S3. The converged free energy surface projected into relevant coordinates is shown in Fig. 5a and the free energy barrier for **EI**→**EIb** is 24.5 kcal mol^{-1}. As expected, the broad nature of the reactant basin along the coordinate $d[AztC_2 - W_1O]$ can be seen in Fig. 5a and thus these results again show the importance of using TASS in modeling this reaction.

While analyzing the trajectories, we noticed that the hydrogen bonding interactions between Lys_{67} and Tyr_{150} is broken as soon as the latter abstracts a proton from W_1; this is clear from different projections of the high-dimensional free energy landscape in Fig. 5b. Most importantly, we notice that Lys_{67} comes close to Ser_{64}, which is stabilized by the formation of hydrogen bonding interaction between Lys_{67} and Ala_{220}. This highlights the crucial role that Ala_{220} plays in facilitating the deacylation reaction. We made similar observation during the mechanistic study of deacylation reaction of cephalothin catalyzed by CBL.[71] Interestingly, we find that the interactions between Lys_{315} and Tyr_{150} was broken in the initial stages of the reaction. As a result of these structural changes, a second layer

water molecule (W_2) moved into the active site. Breaking of Tyr_{150} and Lys_{315} interaction during the deacylation is consistent with the previous two studies.[71,81]

The Azt O_9 was within the oxyanion hole formed by the backbone NH of Ser_{64} and Ser_{318} till W_1 attacks Azt C_2. After the attack of W_1, the negative charge formed on O_9 is stabilized by Ser_{318} NH (backbone) and the substrate Azt N_1–H interactions.

Along $d[\mathrm{AztC_2 - W_1O}]$ coordinate, in the range of 5 Å to 2.5 Å, the free energy surface is flat (see Fig. 5a,b), while for the distances less than 2.4 Å, free energy surface becomes quite steep. The origin of this steepness is important to understand the factors contributing to the origin of high deacylation barrier for aztreonam (compared to other non mono–bactam drugs). Analyses show that W_1 experience steric interactions with the methyl group at C_4 of aztreonam, as W_1 approaches C_2. This can be seen in Fig. 5e, in a snapshot from an umbrella window near the transition state of the reaction: van der Waals spheres on W_1 and methyl show overlap. It is interesting to note that the position of methyl group in aztreonam is occupied by a H atom in other drug molecules such as cephalosporins which are known to deacylate quickly. Previously, on the basis of crystal structure, it was inferred that methyl group at C_4 blocks the attack of hydrolytic water to the ester linkage by providing steric hindrance.[82] This is in agreement with our computations.

Dissociation of EIb to EI

For a qualitative understanding of the overall kinetics of hydrolysis, we need to compute the free energy barriers for the dissociation of **EIb**, i.e. the barriers for both **EIb**→**EI** and **EIb**→**EP**. In this section, we present the results of our simulation of **EIb** → **EI** using the TASS method. Although, this barrier can be obtained from the free energy surface Fig. 5a of **EI** → **EIb**, we recomputed this by an independent simulation to affirm the results. For this simulation, we chose five CVs (see Fig. 2b,c for labeling): (a) the distance of $Tyr_{150}O_\eta$ to W_1O, $d[\mathrm{Tyr_{150}O_\eta - W_1O}]$. (b) coordination number of W_1O to the hydrogen which was transferred to $Tyr_{150}O_\eta$ during the formation of **EIb**, $C[\mathrm{W_1O - W_1H}]$; (c) distance between

$AztC_2$ and W_1O, $d[AztC_2 - W_1O]$; (d) the distance of $Tyr_{150}O_\eta$ to $Lys_{67}N_\zeta$, $d[Tyr_{150}O_\eta - Lys_{67}N_\zeta]$; (e) the distance $Tyr_{150}O_\eta$ and $Lys_{315}N_\zeta$, $d[Tyr_{150}O_\eta - Lys_{315}N_\zeta]$. Out of the five, the last three CVs (c)-(e) were also used in the simulation for **EI→EIb** (in the previous section). The CV, $d[Tyr_{150}O_\eta - W_1O]$ was chosen to simulate different orientations of water molecule W_1 with respect to Tyr_{150}. $C[W_1O - W_1H]$ was chosen as a CV to accelerate proton transfer from $Tyr_{150}O_\eta$ to water. Although we don't expect a broad reactant well along the $d[AztC_2 - W_1O]$ coordinate, we chose to apply the umbrella bias potential along this coordinate for a better control on the reaction sequence and to avoid exchange of water molecules W_1 and W_2 (where W_2 is the water molecule which diffused into the active site after the formation of **EIb**). Metadynamics bias was applied along the $C[W_1O - W_1H]$ coordinate. Other technical details of this TASS simulation are the same as that we used for modeling **EI→EIb**.

We could model the reaction successfully using the TASS method. Reconstructed free energy surface is shown in Fig. 6. In this simulation, we did not sample **EI** exhaustively as we were only interested in computing the barrier for **EIb→EI**. The converged free energy barrier for the **EIb** → **EI** reaction is 3.6 kcal mol^{-1}. The estimate for this barrier from Fig. 5a is also nearly the same (3.5 kcal mol^{-1}).

Formation of EP from EIb

Proton transfer to $Ser_{64}O_\gamma$ is the final step involved in the deacylation of the acyl–enzyme complex **EIb**. To model this reaction in a TASS simulation, we considered three CVs: (a) distance between $Ser_{64}O_\gamma$ and $AztC_2$, $d[Ser_{64}O - AztC_2]$; (b) coordination number of $Ser_{64}O_\gamma$ to the terminal protons of $Lys_{67}N_\zeta$, $C[Ser_{64}O_\gamma - Lys_{67}N_\zeta H_\zeta]$; (c) coordination number of $AztO_9$ to the proton of $AztN_1$; Here, $d[Ser_{64}O - AztC_2]$ was chosen to accelerate bond breaking between $Ser_{64}O_\gamma$ and $AztC_2$ and we applied umbrella bias along this coordinate. Umbrella windows were placed from 1.3 Å to 2.8 Å at an interval of 0.1 Å. The coordinate $C[Ser_{64}O_\gamma - Lys_{67}N_\zeta H_\zeta]$ was chosen to accelerate the proton transfer from Lys_{67} to Ser_{64},

and this coordinate was chosen for applying the metadynamics bias potential. The third CV was chosen to disturb the oxyanion-hole present in the **EIb** structure, where the $AztO_9$ is in hydrogen bonding interaction with the proton of $AztN_1$, which stabilizes this intermediate.

We successfully simulated this process using above defined set of CVs and barrier associated for this process is 6.5 kcal mol^{-1} (Fig. 7c). We have seen proton transfer from Lys_{67} to $Ser_{64}O_\gamma$ followed by the breakage of C_2–O_γ bond.

The reconstructed free energy surface from TASS simulation is given in Fig. 7a. The free energy barrier for this process is found to be 6.5 kcal mol^{-1}, which differs only by 1 kcal mol^{-1} to the free energy barrier computed using a conventional MTD simulation (7.5 kcal mol^{-1}; see SI Section 4.

Conclusions and Discussions

Based on the results of this study, combined with our earlier results for acylation,[62] we predict the overall mechanism and kinetics of aztreonam hydrolysis by CBL. From Fig. 8, the effective free energy barrier for the deacylation step **EI**→**EP** is 27.5 kcal mol^{-1} while that for the reverse-acylation step **EI**→**ES** is 25.6 kcal mol^{-1}. These barriers are higher than that for the acylation (**ES**→**EI**), which is 22 kcal mol^{-1}. It is clear from the free energy profile in Fig. 8 that the effective free energy barrier for **EI**→**ES** is nearly the same as that for **EI**→**EP**. To be exact, the free energy barrier for **EI**→**EP** is slightly larger than **EI**→**ES** , which implies that acylation of aztreonam is reversible. However, the free energy barriers for these two competing decay routes differ only by 2 kcal mol^{-1}, which is close to the error in the methods we used.[62] Thus more careful experimental kinetics study would be necessary to verify the reversibility of acylation. In fact, reverse acylation is reported for inhibitors such as avibactam with CBL and other beta-lactamases.[61]

On comparing these results with the deacylation kinetics for cephalothin,[62] as in our previous study (using the same QM/MM techniques), we deduce that hydrolysis of aztre-

onam, in particular, the deacylation step, is slower than that of cephalothin. This is also in agreement with the experimental kinetics results.[50,58] The free energy profile in Fig. 8 shows that deacylation step is the rate determining step in the aztreonam hydrolysis, implying that $k_{\mathrm{cat}} \approx k_3$, if deacylating, else $k_{\mathrm{cat}} \approx k_{-2}$ if reverse-acylating. On the other hand, for cephalothin hydrolysis, our earlier study found that acylation step is the rate-determining, and $k_{\mathrm{cat}} \approx k_2$. These results affirm the special nature of the aztreonam drug and indicate that the drug behaves as a transient inhibitor for CBL. Analysis shows that the origin of slow deacylation in aztreonam is due to the stereochemistry of the methyl substitution at AztC_4. During deacylation, W_1 approaches AztC_2 at distances less than 2.4 Åwhen W_1 faces steric hindrance from the methyl group at AztC_4. This makes nucleophilic attack of W_1 a slower process in the case of aztreonam compared to that of cephalothin. We note in passing that in cephalothin H atom is occupying the position of the methyl group in aztreonam. This is an important result as it demonstrates that methyl substitution at the C_4 position can slow down the deacylation reaction.

Overall, we have demonstrated the effectiveness of the TASS method in combination with hybrid QM/MM simulations to obtain insights on the mechanism and kinetics of hydrolysis of aztreonam drug catalyzed by CBL. The efficiency of TASS method in the exploration of high dimensional free energy surfaces can be seen in the cases of reverse acylation and deacylation reactions where more than 3 CVs were used for enhanced sampling. Most importantly, we are able to achieve reliable free energy estimates that converge systematically with simulation time. Quick convergence in the free energy estimates is by the virtue of enhanced sampling of large number of CVs. We hope that the technical details of TASS simulations and choice of CVs given here will be useful for the future application of the TASS method to study enzymatic reactions using QM/MM based MD simulations.

Acknowledgement

S.A. is thankful to University Grant Commission, India, and Department of Biotechnology, India, for funding her Ph.D. program. This work is part of the sponsored project by Department of Biotechnology. Authors used HPC facilities at the Department of Chemistry and Computer Center, IIT Kanpur.

Supporting Information Available

This material is available free of charge via the Internet at `http://pubs.acs.org/`.

References

(1) Peters, B. *Reaction Rate Theory and Rare Events*; Elsevier: Amsterdam, Netherlands, 2017.

(2) Tuckerman, M. E. *Statistical Mechanics: Theory and Molecular Simulation*, 1st ed.; Oxford University Press: Oxford, 2010.

(3) Lelièvre, T.; Rousset, M.; Stoltz, G. *Free Energy Computations: A Mathematical Perspective*; Imperial College Press: London, 2010.

(4) Laio, A.; Parrinello, M. Escaping Free-energy Minima. *Proc. Natl. Acad. Sci. U.S.A* **2002**, *99*, 12562.

(5) Huber, T.; Torda, A. E.; van Gunsteren, W. F. Local elevation: A Method for Improving the Searching Properties of Molecular Dynamics Simulation. *J. Comput. Aided Mol. Des.* **1994**, *8*, 695.

(6) Wang, F.; Landau, D. P. Efficient, Multiple-Range Random Walk Algorithm to Calculate the Density of States. *Phys. Rev. Lett.* **2001**, *86*, 2050.

(7) Hansmann, U. H. E.; Wille, L. T. Global Optimization by Energy Landscape Paving. *Phys. Rev. Lett.* **2002**, *88*, 068105.

(8) Darve, E.; Pohorille, A. Calculating Free Energies Using Average Force. *J. Chem. Phys.* **2001**, *115*, 9169.

(9) Comer, J.; Gumbart, J. C.; Hénin, J.; Lelièvre, T.; Pohorille, A.; Chipot, C. The Adaptive Biasing Force Method: Everything You Always Wanted To Know but Were Afraid To Ask. *J. Phys. Chem. B* **2015**, *119*, 1129.

(10) Maragliano, L.; Vanden-Eijnden, E. A Temperature Accelerated Method for Sampling Free Energy and Determining Reaction Pathways in Rare Events Simulations. *Chem. Phys. Lett.* **2006**, *426*, 168.

(11) Chen, M.; Cuendet, M. A.; Tuckerman, M. E. Heating and Flooding: A Unified Approach for Rapid Generation of Free Energy Surfaces. *J. Chem. Phys.* **2012**, *137*, 024102.

(12) Cuendet, M. A.; Tuckerman, M. E. Free Energy Reconstruction from Metadynamics or Adiabatic Free Energy Dynamics Simulations. *J. Chem. Theory Comput.* **2014**, *10*, 2975.

(13) Chen, M.; Yu, T.-Q.; Tuckerman, M. E. Locating Landmarks on High-Dimensional Free Energy Surfaces. *Proc. Natl. Acad. Sci.* **2015**, *112*, 3235.

(14) Morishita, T.; Itoh, S. G.; Okumura, H.; Mikami, M. Free-Energy Calculation Via Mean-force Dynamics Using a Logarithmic Energy Landscape. *Phys. Rev. E* **2012**, *85*, 066702.

(15) Barducci, A.; Bussi, G.; Parrinello, M. Well-Tempered Metadynamics: A Smoothly Converging and Tunable Free-Energy Method. *Phys. Rev. Lett.* **2008**, *100*, 020603.

(16) Barnett, C. B.; Naidoo, K. J. Free Energies from Adaptive Reaction Coordinate Forces (FEARCF): An Application to Ring Puckering. *Mol. Phys.* **2009**, *107*, 1243–1250.

(17) Vanden-Eijnden, E. Some Recent Techniques for Free Energy Calculations. *J. Comput. Chem.* **2009**, *30*, 1737.

(18) Christ, C. D.; Mark, A. E.; van Gunsteren, W. F. Basic Ingredients of Free Energy Calculations: A Review. *J. Comput. Chem.* **2010**, *31*, 1569.

(19) Abrams, C.; Bussi, G. Enhanced Sampling in Molecular Dynamics Using Metadynamics, Replica-Exchange, and Temperature-Acceleration. *Entropy* **2014**, *16*, 163.

(20) Torrie, G. M.; Valleau, J. P. Monte Carlo Free Energy Estimates Using Non-Boltzmann Sampling: Application to the Sub-critical Lennard-Jones Fluid. *Chem. Phys. Lett.* **1974**, *28*, 578.

(21) Valsson, O.; Tiwary, P.; Parrinello, M. Enhancing Important Fluctuations: Rare Events and Metadynamics from a Conceptual Viewpoint. *Annu. Rev. Phys. Chem.* **2016**, *67*, 159.

(22) Kästner, J. Umbrella Sampling. *WIREs Comput. Mol. Sci.* **2011**, *1*, 932.

(23) Barducci, A.; Bonomi, M.; Parrinello, M. Metadynamics. *WIREs Comput. Mol. Sci.* **2011**, *1*, 826.

(24) Sutto, L.; Marsili, S.; Gervasio, F. L. New Advances in Metadynamics. *WIREs: Comput. Mol. Sci.* **2012**, *2*, 771.

(25) Bussi, G.; Gervasio, F. L.; Laio, A.; Parrinello, M. Free-Energy Landscape for β Hairpin Folding from Combined Parallel Tempering and Metadynamics. *J. Am. Chem. Soc.* **2006**, *128*, 13435.

(26) Gil-Ley, A.; Bussi, G. Enhanced Conformational Sampling Using Replica Exchange with Collective-Variable Tempering. *J. Chem. Theory Comput.* **2015**, *11*, 1077.

(27) Abrams, J. B.; Tuckerman, M. E. Efficient and Direct Generation of Multidimensional Free Energy Surfaces via Adiabatic Dynamics without Coordinate Transformations. *J. Phys. Chem. B* **2008**, *112*, 15742.

(28) Pfaendtner, J.; Bonomi, M. Efficient Sampling of High-Dimensional Free-Energy Landscapes with Parallel Bias Metadynamics. *J. Chem. Theory Comput.* **2015**, *11*, 5062.

(29) Piana, S.; Laio, A. A Bias-Exchange Approach to Protein Folding. *The Journal of Physical Chemistry B* **2007**, *111*, 4553.

(30) Awasthi, S.; Nair, N. N. Exploring High Dimensional Free Energy Landscapes: Temperature Accelerated Sliced Sampling. *J. Chem. Phys.* **2017**, *146*, 094108.

(31) Valsson, O.; Parrinello, M. Variational Approach to Enhanced Sampling and Free Energy Calculations. *Phys. Rev. Lett.* **2014**, *113*, 090601.

(32) Shaffer, P.; Valsson, O.; Parrinello, M. Enhanced, targeted sampling of high-dimensional free-energy landscapes using variationally enhanced sampling, with an application to chignolin. *Proc. Natl. Acad. Sci.* **2016**, *113*, 1150.

(33) Awasthi, S.; Kapil, V.; Nair, N. N. Sampling Free Energy Surfaces as Slices by Combining Umbrella Sampling and Metadynamics. *J. Comput. Chem.* **2016**, *37*, 1413.

(34) Ferrenberg, A. M.; Swendsen, R. H. Optimized Monte Carlo Data Analysis. *Phys. Rev. Lett.* **1989**, *63*, 1195.

(35) Kumar, S.; Rosenberg, J. M.; Bouzida, D.; Swendsen, R. H.; Kollman, P. A. The Weighted Histogram Analysis Method for Free-energy Calculations on Biomolecules. I. The Method. *J. Comput. Chem.* **1992**, *13*, 1011.

(36) Bonomi, M.; Barducci, A.; Parrinello, M. Reconstructing the Equilibrium Boltzmann Distribution from Well-tempered Metadynamics. *J. Comput. Chem.* **2009**, *30*, 1615.

(37) Tiwary, P.; Parrinello, M. A Time-Independent Free Energy Estimator for Metadynamics. *J. Phys. Chem. B* **2014**, *119*, 736.

(38) Zaman, S. B.; Hussain, M. A.; Nye, R.; Mehta, V.; Mamun, K. T.; ; Hossain, N. A Review on Antibiotic Resistance: Alarm Bells are Ringing. *Cureus* **2017**, *9*, e1403.

(39) O'Neill, J. Tackling Drug-Resistant Infections Globally: Final Report and Recommendations. *Review on Antimicrobial Resistance* **2016**,

(40) Holmes, A. H.; Moore, L. S. P.; Sundsfjord, A.; Steinbakk, M.; Regmi, S.; Karkey, A.; Guerin, P. J.; Piddock, L. J. V. Understanding the Mechanisms and Drivers of Antimicrobial Resistance. *The Lancet* **2016**, *387*, 176.

(41) WHO, *Antimicrobial Resistance: Global Report on Surveillance 2014*; WHO Press, World Health Organization: Geneva, 2014.

(42) Davies, J.; Davies, D. Origins and Evolution of Antibiotic Resistance. *Microbiol. Mol. Biol. Rev.* **2010**, *74*, 417.

(43) Alanis, A. J. Resistance to Antibiotics: Are We in the Post-Antibiotic Era? *Archives of Medical Research* **2005**, *36*, 697.

(44) Waxman, D. J.; Strominger, J. L. Penicillin-Binding Proteins and the Mechanism of Action of Beta-Lactam Antibiotics. *Annu. Rev. Biochem.* **1983**, *52*, 825.

(45) Zapun, A.; Contreras-Martel, C.; Vernet, T. Penicillin-binding Proteins and β-Lactam Resistance. *FEMS Microbiol. Rev.* **2008**, *32*, 361.

(46) Ambler, R. P. The Structure of β-Lactamases. *Phil. Trans. R. Soc. Lond. B* **1980**, *289*, 321.

(47) Sanders, C. C.; Sanders, W. E. Clinical Importance of Inducible Beta-Lactamases in Gram-Negative Bacteria. *Eur. J. Clin. Microbiol.* **1987**, *6*, 435.

(48) Sanders, C. C.; Sanders, W. E. β-Lactam Resistance in Gram-Negative Bacteria: Global Trends and Clinical Impact. *Clin. Infect. Dis.* **1992**, *15*, 824.

(49) Majiduddin, F. K.; Materon, I. C.; Palzkill, T. G. Molecular analysis of beta-lactamase structure and function. *Int. J. Med. Microbiol.* **2002**, *292*, 127.

(50) Monnaie, D.; Virden, R.; Frère, J. M. A Rapid-Kinetic Study of the Class-C β-Lactamase of Enterobacter Cloacae 908R. *FEBS Letters* **1992**, *306*, 108.

(51) Cavalli, A.; Carloni, P.; Recanatini, M. Target-Related Applications of First Principles Quantum Chemical Methods in Drug Design. *Chem. Rev.* **2005**, *106*, 3497.

(52) Gaoo, K.-S.; Sim, T.-S. Designing New β-Lactams: Implications from Their Targets, Resistance Factors and Synthesizing Enzymes. *Curr. Comp. Aided–Drug Design* **1011**, *7*, 53.

(53) Tsukamoto, K.; Tachibana, K.; Yamazaki, N.; Ishii, Y.; Ujiie, K.; Nishida, N.; Sawai, T. Role of Lysine-67 in the Active Site of Class C β–Lactamase from Citrobacter Freundii GN346. *Eur. J. Biochem.* **1990**, *188*, 15.

(54) Tsukamoto, K.; Nishida, N.; Tsuruoka, M.; Sawai, T. Function of the Conserved Triad Residues in the Class C β-Lactamase from Citrobacter Freundii GN346. *FEBS Lett.* **1990**, *271*, 243.

(55) Monnaie, D.; Dubus, A.; Frère, J.-M. The Role of Lysine-67 in a Class C β-Lactamase is Mainly Electrostatic. *Biochem. J.* **1994**, *302*, 1.

(56) Monnaie, D.; Dubus, A.; Cooke, D.; Marchand-Brynaert, J.; Normark, S.; Frère, J.-M. Role of Residue Lys315 in the Mechanism of Action of the Enterobacter cloacae 908R β–Lactamase. *Biochemistry* **1994**, *33*, 5193.

(57) Dubus, A.; Ledent, P.; Lamotte-Brasseur, J.; Frère, J.-M. The Roles of Residues Tyrl50,

Glu272, and His314 in Class C β-Lactamases. *Proteins: Struct., Funct., Genet.* **1996**, *25*, 473.

(58) Galleni, M.; Amicosante, G.; Frère, J. M. A Survey of the Kinetic Parameters of Class C β-lactamases. Cephalosporins and Other β-lactam Compounds. *Biochemical Journal* **1988**, *255*, 123.

(59) Tripathi, R.; Nair, N. N. Deacylation Mechanism and Kinetics of Acyl–Enzyme Complex of Class C β-Lactamase and Cephalothin. *J. Phys. Chem. B* **2016**, *120*, 2681.

(60) Buynak, J. D. Understanding the Longevity of the β-Lactam Antibiotics and of Antibiotic/β-Lactamase Inhibitor Combinations. *Biochem. Pharmacol.* **2006**, *71*, 930.

(61) Lahiri, S. D.; Johnstone, M. R.; Ross, P. L.; McLaughlin, R. E.; Olivier, N. B.; Alm, R. A. Avibactam and Class C β-Lactamases: Mechanism of Inhibition, Conservation of the Binding Pocket, and Implications for Resistance. *Antimicrob. Agents Chemother.* **2014**, *58*, 5704.

(62) Tripathi, R.; Nair, N. N. Mechanism of Acyl–enzyme Complex Formation from the Henry–Michaelis Complex of Class C β-Lactamases with β-Lactam Antibiotics. *J. Am. Chem. Soc.* **2013**, *135*, 14679.

(63) Oefner, C.; D'Arcy, A.; Daly, J. J.; Gubernator, K.; Charnas, R. L.; Heinze, I.; Hubschwerlen, C.; Winkler, F. K. Refined crystal structure of β-lactamase from Citrobacter freundii indicates a mechanism for β-lactam hydrolysis. *Nature* **1990**, *343*, 284.

(64) Version 13.2, `CPMD` Program Package. IBM Corp 1990-2018, MPI für Festkörperforschung Stuttgart 1997-2018.

(65) Cheatham III, T. E.; Cieplak, P.; Kollman, P. A. A Modified Version of the Cornell et al. Force Field with Improved Sugar Pucker Phases and Helical Repeat. *J. Biomol. Struct. Dyn.* **1999**, *16*, 845–862.

(66) Perdew, J. P.; Chevary, J. A.; Vosko, S. H.; Jackson, K. A.; Pederson, M. R.; Singh, D. J.; Fiolhais, C. Atoms, Molecules, Solids, and Surfaces: Applications of the Generalized Gradient Approximation for Exchange and Correlation. *Phys. Rev. B* **1992**, *46*, 6671.

(67) Vanderbilt, D. Soft Self-Consistent Pseudopotentials in a Generalized Eigenvalue Formalism. *Phys. Rev. B* **1990**, *41*, 7892.

(68) Laio, A.; VandeVondele, J.; Rothlisberger, U. A Hamiltonian Electrostatic Coupling Scheme for Hybrid Car-Parrinello Molecular Dynamics Simulations. *J. Chem. Phys.* **2002**, *116*, 6941.

(69) Martyna, G. J.; Klein, M. L.; Tuckerman, M. Nosé–Hoover chains: The Canonical Ensemble via Continuous Dynamics. *J. Chem. Phys.* **1992**, *97*, 2635.

(70) Car, R.; Parrinello, M. Unified Approach for Molecular Dynamics and Density-Functional Theory. *Phys. Rev. Lett.* **1985**, *55*, 2471.

(71) Tripathi, R.; Nair, N. N. Deacylation Mechanism and Kinetics of Acyl–Enzyme Complex of Class C β–Lactamase and Cephalothin. *J. Phys. Chem. B* **2016**, *120*, 2681.

(72) Lammote-Brasseur, J.; Dubus, A.; Wade, R. C. pK_a Calculations for Class C β-lactamase: The Role of Tyr-150. *Proteins: Struct., Funct., Genet.* **2000**, *40*, 23.

(73) Lobkovsky, E.; Billings, E. M.; Moews, P. C.; Rahil, J.; Pratt, R. F.; Knox, J. R. Crystallographic Structure of a Phosphonate Derivative of the Enterobacter Cloacae P99 Cephalosporinase: Mechanistic Interpretation of a β-Lactamase Transition-State Analog. *Biochemistry* **1994**, *33*, 6762.

(74) Patera, A.; Blaszczak, L. C.; Shoichet, B. K. Crystal Structures of Substrate and Inhibitor Complexes with AmpC β-Lactamase: Possible Implications for Substrate-Assisted Catalysis. *J. Am. Chem. Soc.* **2000**, *122*, 10504.

(75) Powers, R. A.; Shoichet, B. K. Structure-Based Approach for Binding Site Identification on AmpC β–Lactamase. *J. Med. Chem.* **2002**, *45*, 3222.

(76) Wouters, J.; Fonze, E.; Vermeire, M.; Frere, J.; Charlier, P. Crystal Structure of Enterobacter Cloacae 908R Class C β-Lactamase Bound to Iodo-acetamido-phenyl Boronic acid, a Transition-state Analogue. *Cell. Mol. Life Sci.* **2003**, *60*, 1764.

(77) Chen, Y.; Minasov, G.; Roth, T. A.; Prati, F.; Shoichet, B. K. The Deacylation Mechanism of AmpC β-Lactamase at Ultrahigh Resolution. *J. Am. Chem. Soc.* **2006**, *128*, 2970.

(78) Kato-Toma, Y.; Iwashita, T.; Masuda, K.; Oyama, Y.; Ishiguru, M. pK_a Measurements from Nuclear Magnetic Resonance of Tyrosine-150 in Class C β-Lactamase. *Biochem. J.* **2003**, *371*, 175.

(79) Bulychev, A.; Massova, I.; Miyashita, K.; Mobashery, S. Nuances of Mechanisms and Their Implications for Evolution of the Versatile β–Lactamase Activity: From Biosynthetic Enzymes to Drug Resistance Factors. *J. Am. Chem. Soc.* **1997**, *119*, 7619–7625.

(80) Gherman, B. F.; Goldberg, S. D.; Cornish, V. W.; Friesner, R. A. Mixed Quantum Mechanical/Molecular Mechanical (QM/MM) Study of the Deacylation Reaction in a Penicillin Binding Protein (PBP) versus in a Class C β–Lactamase. *J. Am. Chem. Soc.* **2004**, *126*, 7652.

(81) Hata, M.; Tanaka, Y.; Fujii, Y.; Neya, S.; Hoshino, T. A Theoretical Study on the Substrate Deacylation Mechanism of Class C β–Lactamase. *J. Phys. Chem. B* **2005**, *109*, 16153.

(82) Heinze-Krauss, I.; Angehrn, P.; Charnas, R. L.; Gubernator, K.; Gutknecht, E.-M.; Hubschwerlen, C.; Kania, M.; Oefner, C.; Page, M. G. P.; Sogabe, S. et al. Structure-Based Design of β-Lactamase Inhibitors. 1. Synthesis and Evaluation of Bridged Monobactams. *J. Med. Chem.* **1998**, *41*, 3961–3971.

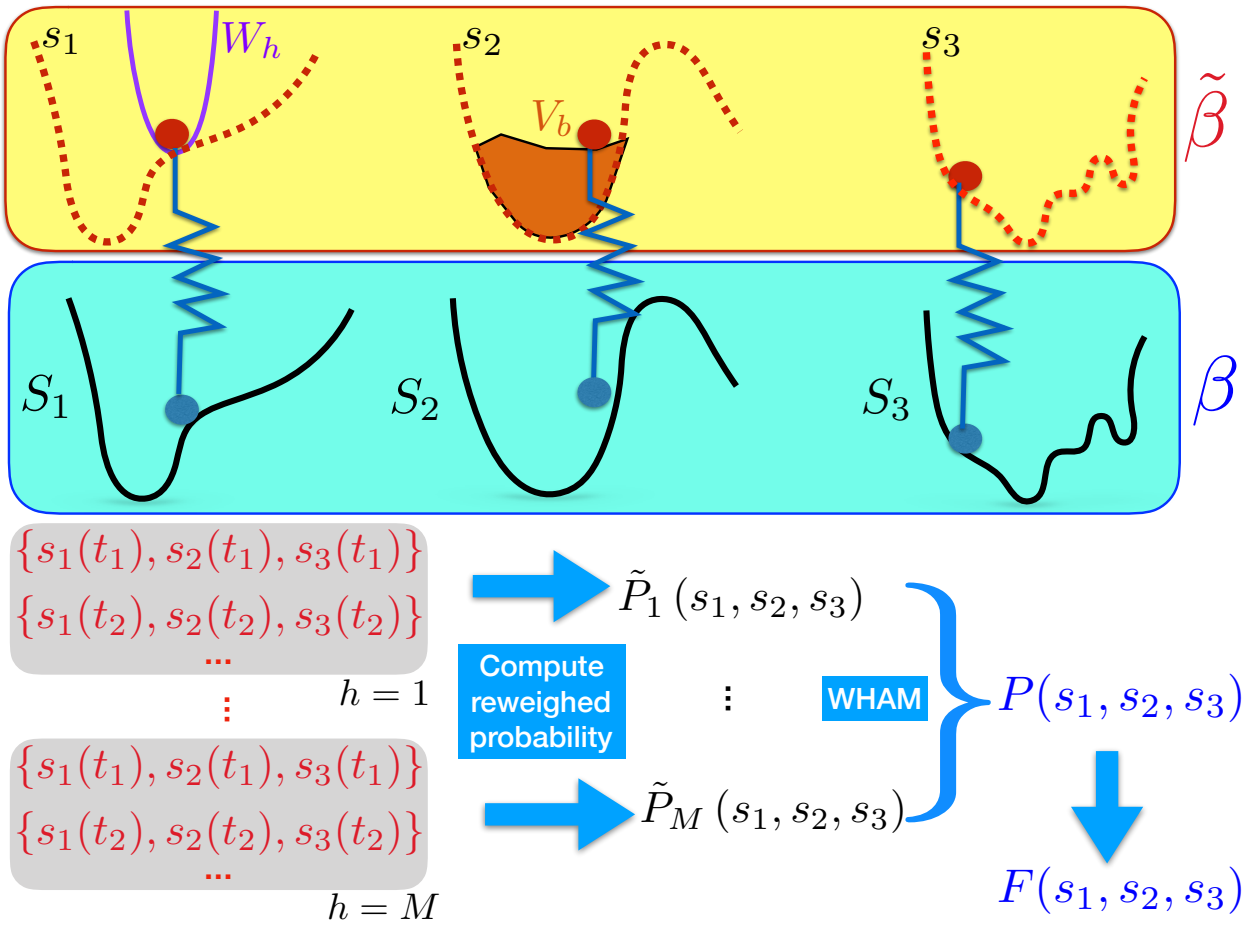

Figure 1: A schematic representation of the TASS Lagrangian for a case with three CVs S_1, S_2, and S_3 is given. In a replica h, umbrella sampling bias potential W_h is applied on the auxiliary variable s_1, and metadynamics bias potential (V_b) is applied on s_2. Moreover, all the auxiliary variables $\{s_\alpha\}$ are connected to a thermostat with inverse temperature $\tilde{\beta} = 1/k_B\tilde{T}$ and the physical system is thermostatted to an inverse temperature $\beta = 1/k_BT$. We choose $\tilde{\beta} << \beta$. Steps involved in getting the combined Boltzmann probability distribution of $\{s_\alpha\}$, $P(\mathbf{s})$, using their biased trajectories from different replicas $h = 1, \cdots, M$ is also shown.

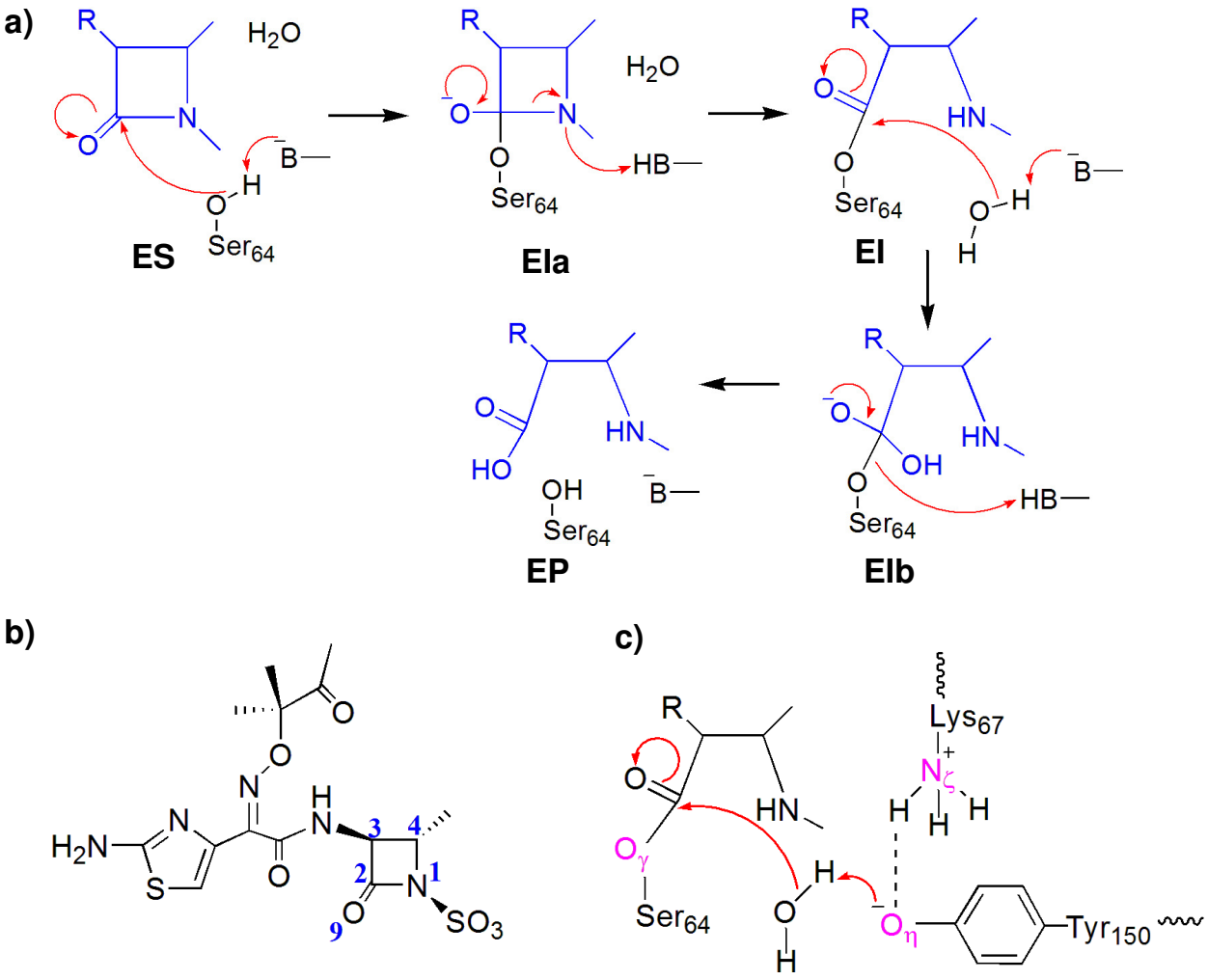

Figure 2: a) General mechanism of hydrolysis of a β-lactam antibiotic (blue in color) catalyzed by CBL. The reaction involves acylation (**ES**→**EI**) and deacylation (**EI**→**EP**) reactions. Here B represents a basic residue within the active site of the enzyme. b) Structure of aztreonam drug; Atom numbers labeled here are used in the main text. c) **EI** structure is shown here and certain atom labels are indicated. Here the arrows correspond to the mechanism of deacylation reaction studied here.

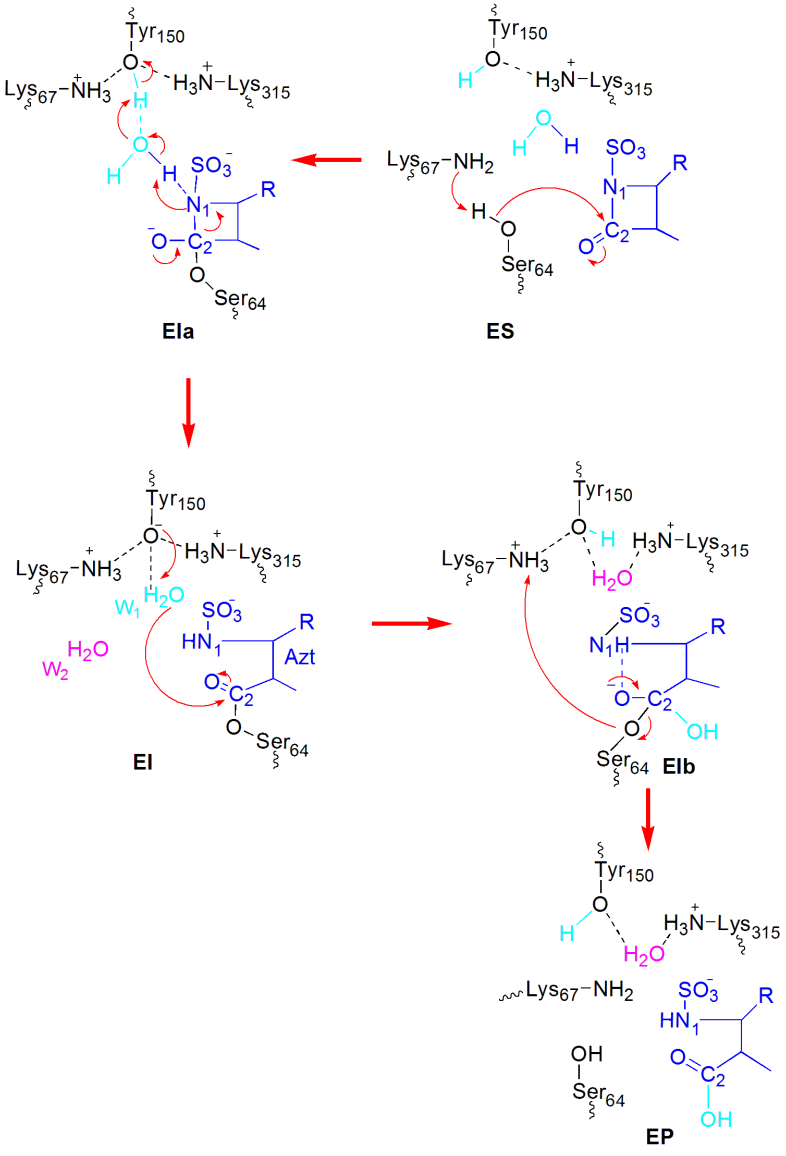

Figure 3: Proposed mechanism of acylation and deacylation reactions of aztreonam by CBL.

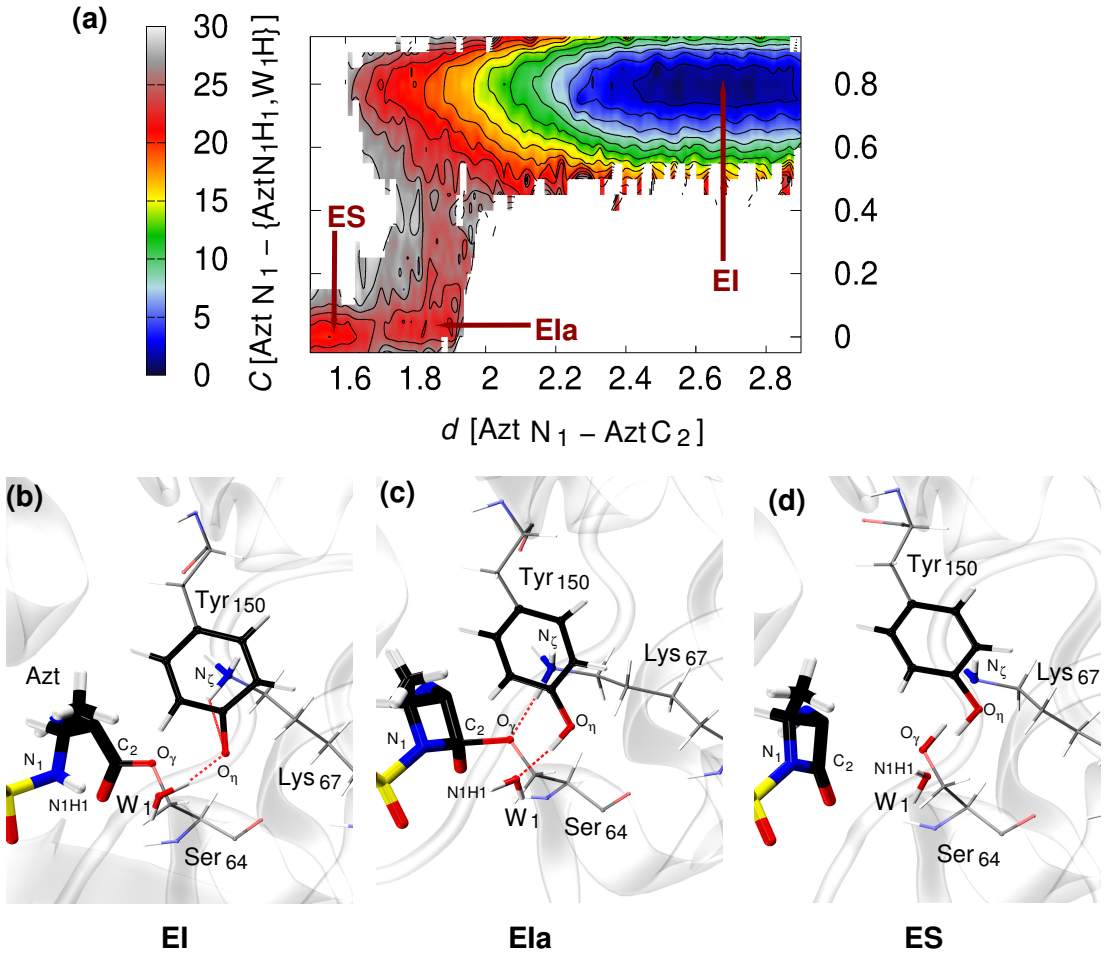

Figure 4: (a) Projected nine dimensional free energy landscape for the reaction **EI**→**ES**; Contour lines are drawn for every 2 kcal mol^{-1}. Here d[AztN$_1$ – AztC$_2$] is in Å. Subfigures (b), (c), and (d) show representative snapshots of **EI**, **EIa**, and **ES** from the QM/MM trajectory. Atom colors: S (yellow), O (red), N (blue), C (black), H (white). Protein backbone is represented as transparent ribbons.

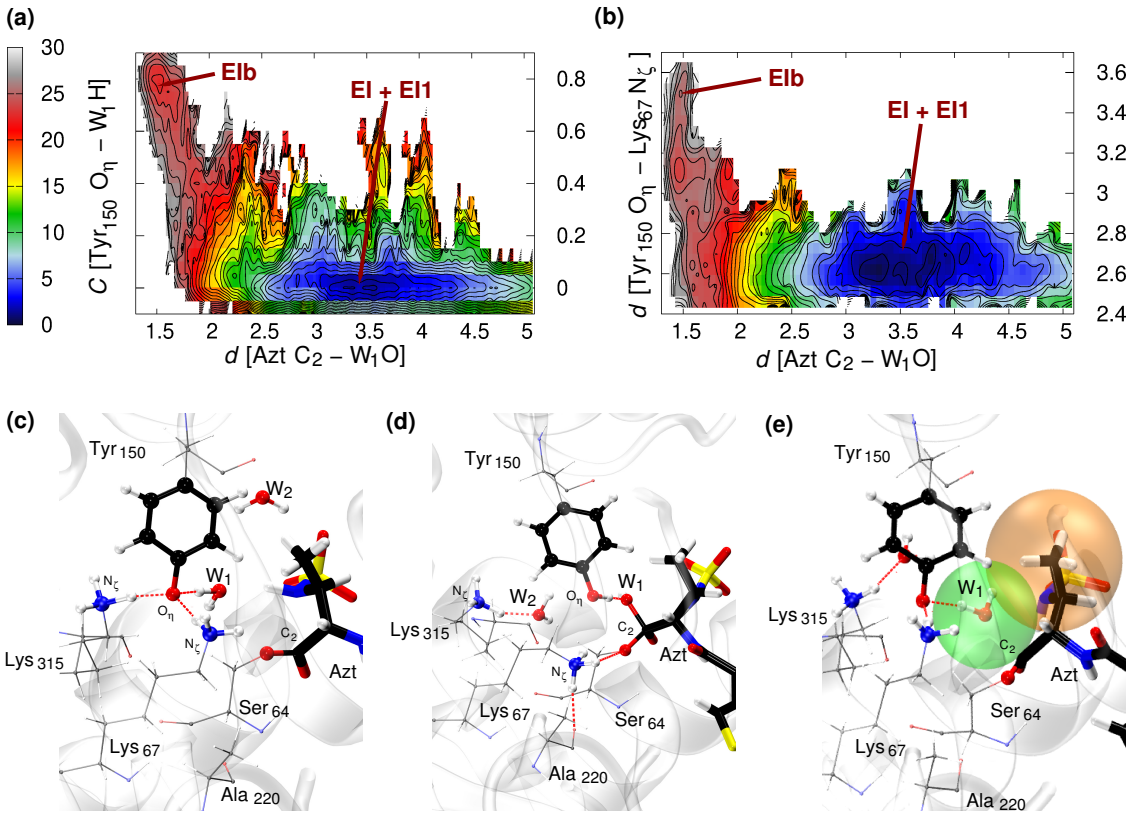

Figure 5: (a) and (b) are the two different projections of the five dimensional free energy landscape as obtained from TASS simulation formation of tetrahedral complex; Contour lines are drawn at every 1 kcal mol^{-1}.[30] Subfigures (c) and (d) show representative snapshots of **EI1** and **EIb** from the trajectory of this simulation, respectively. (e) Snapshot from umbrella window at 2 Å showing steric interaction of CH_3 with W1. Here the green and orange transparent spheres of radius 2 Å and 1.52 Å are drawn on O atom of W1 and C atom of CH_3, respectively, based on their van der Waals radius. Atom colors: S (yellow), O (red), N (blue), C (black), H (white) ; protein backbone is represented as transparent ribbons.

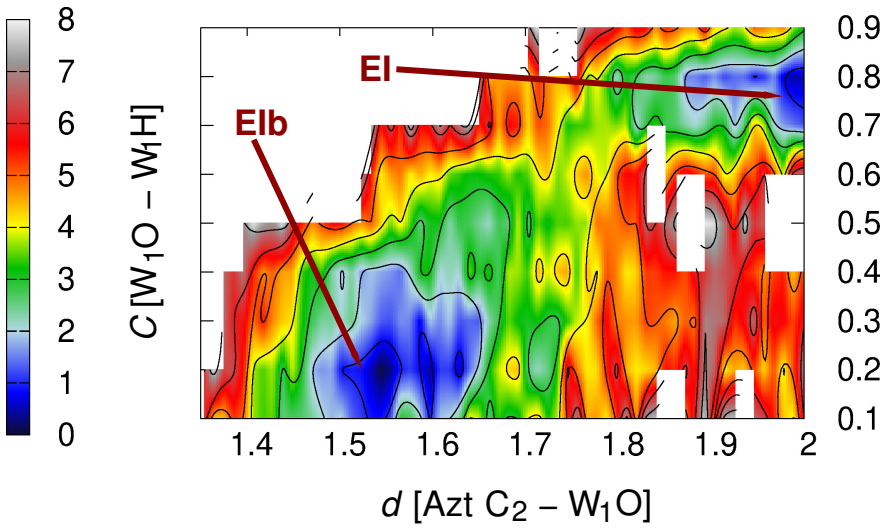

Figure 6: A two–dimensional projection of six dimensional free energy surface as obtained from TASS simulation for **EIb** $\rightarrow$ **EI**. Distance CV is in Å. Contour values are drawn at an interval of 1 kcal mol^{-1}.

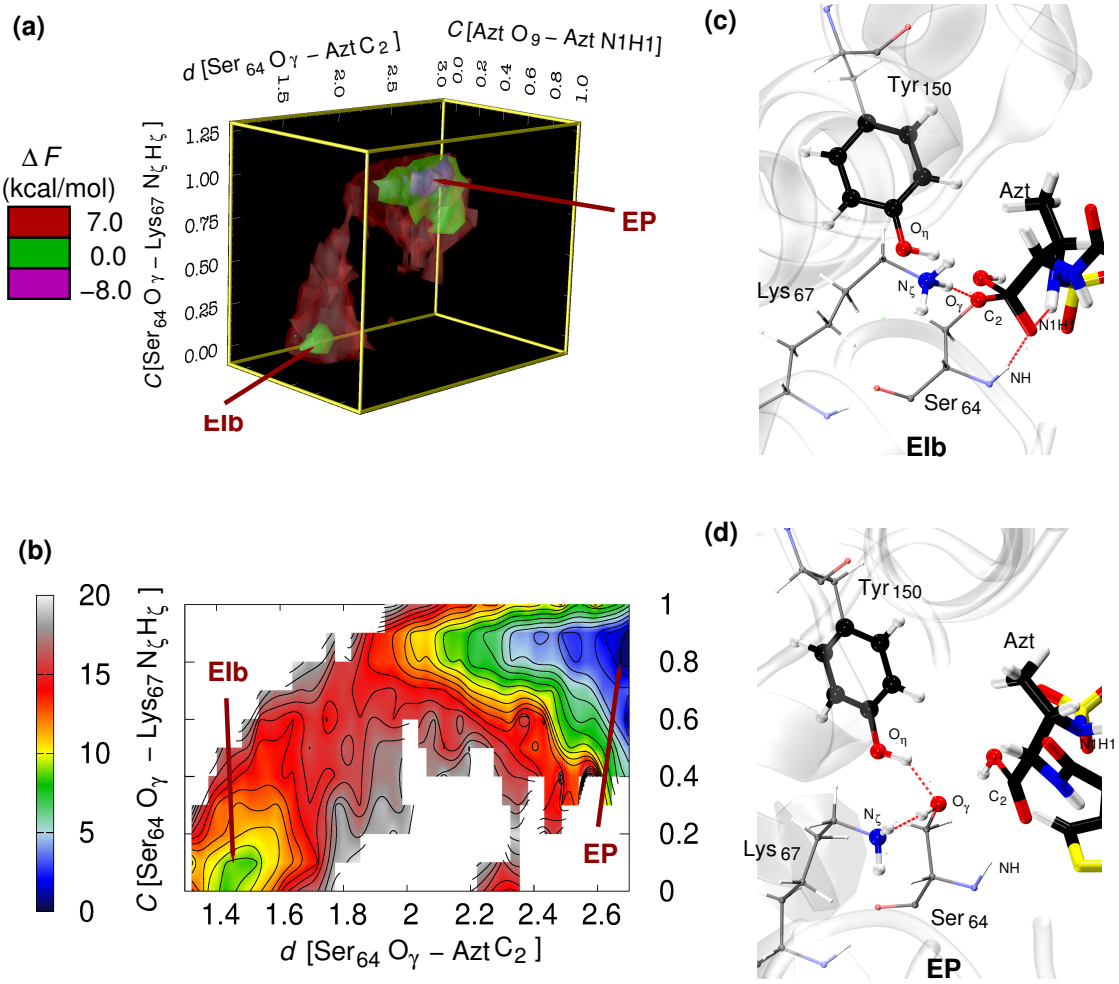

Figure 7: (a) Reconstructed 4–dimensional free energy surface as obtained from the TASS simulation of **EIb** → **EP**; (b) 3–dimensional projection of the 4–dimensional free energy landscape; (c) Reconstructed free energy landscape computed from conventional MTD simulations; Here, distance CVs are in Å; Contour lines are drawn at every 1 kcal mol^{-1}; (d) and (e) show snapshots of **EIb** and **EP** from the TASS simulation. Atom colors: S (yellow), O (red), N (blue), C (black), H (white) ; protein backbone is represented by transparent ribbons.

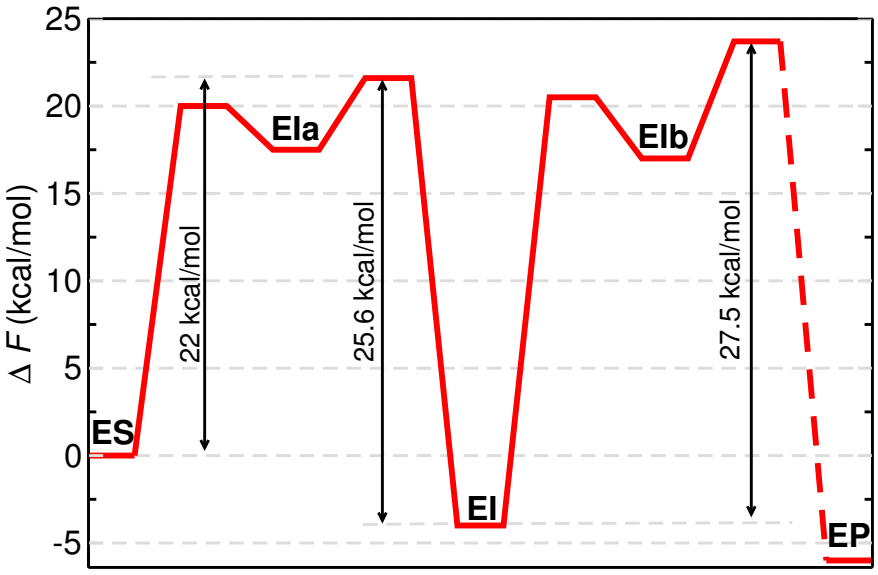

Figure 8: Free energy profile for the aztreonam hydrolysis catalyzed by CBL. Barrier for **ES** to **EI** is taken from.[62] Here, dotted line represents that the barrier is not computed in this work.

TOC Picture:

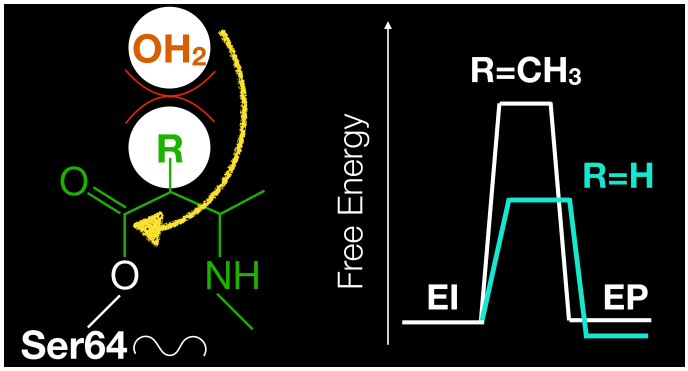

Figure 9: Table of Contents figure.